Hematologic Characterization and 3D Imaging of Red Blood Cells Using a Compressive Nano-Antenna and ML-FMA Modeling

Hipólito Gómez-Sousa[1], Óscar Rubiños-López[1], José Ángel Martínez-Lorenzo[2]

[1]Department of Signal Theory and Communications, University of Vigo, EI de Telecomunicación,
Campus Universitario, E-36310 Vigo, Spain.

[2]Northeastern University, 360 Huntington Ave, Suite 302 Stearns Center, Boston, MA 02115, USA.

Abstract—In vivo **sensing and imaging of human tissues using micro- and/or nano-sensing platforms constitutes one of the biggest challenges in the field of bioengineering for the next several years or decades. Such sensing platforms mounted on micro- or nano- robots not only will enable real-time monitoring of biological tissues, but it may also play a pivotal role in the localization and treatment of cancerous cells inside of the human body. Enabled by the recent development of novel Compressive Antennas, in this paper we present some preliminary results showing the feasibility of hematologic characterization and 3D imaging of red blood cells affected by different disorders using a nano-sensing electromagnetic platform operating at optical frequencies.**

*Index Terms—***red blood cells, computational electromagnetics, multilevel fast multipole algorithm, electromagnetic scattering, compressive sensing**

I. INTRODUCTION

Hematologic characterization of human red blood cells (RBCs) using electromagnetic radiation has been recently proposed as an appealing technique for the diagnosis of blood disorders at optical frequencies [1–4]. Accurate electromagnetic characterization of such blood disorders require the use of advanced Computational Electromagnetic (CEM) codes. In [1, 2], volumetric computational methods were used to characterize the scattering of RBC. Specifically, the finite-difference time-domain (FDTD) method was used in [1], whereas the invariant imbedding T-matrix method (II-TM) and the discrete-dipole approximation (DDA) method were chosen for [2]. Despite these volumetric approaches are widely used in CEM community, they cannot manage electrically-large simulations encountered in realistic applications. In [3], a simulation environment based on the multilevel fast multipole algorithm (MLFMA) was used in order to enalable electrically-large simulations. A description of the MLFMA can be found in [5,6]. Unlike volumetric approaches hereinabove commented, the MLFMA only requires a triangular discretization of the RBC surfaces and drastically reduces the computational requirements. Nonetheless, the MLFMA simulations described in [3] were performed on isolated RBCs, not on full blood samples. As a result, a large number of measurements of scattering angles are required by the simulated setup for an accurate characterization.

Real experiments with RBCs involving quantitative phase imaging (QPI) techniques have been reported in [4]. The measurements in [4] were also performed on individual RBCs, therefore presenting the same computational limitation described before. Additionally, the experimental imaging setup was based on using bulky lenses and cameras, which limited its use only for *in vitro* tests.

This work presents a preliminary study on hematologic characterization and 3D imaging of RBCs affected by different disorders. On one hand, the hematologic characterization is performed in terms of the Radar Cross Section(RCS) or Scattering Cross Section (SCS) of well-defined solutions containing several RBCs affected by different disorders. On the other hand, the 3D imaging of RBC's is performed by making use of a novel Compressive Nano-antenna, which leverages on the field of compressive sensing and multidimensional codification to reduce the cost, energy-budget and space needed to perform real-time imaging [7–10]. The Compressive Antenna was originally proposed to perform imaging at millimiter wave frequencies for security applications [9–10]; however, the same design methodology is still valid to be applied in the micro- and/or nano- scale domains. As a result, the proposed Compressive Nano-Antenna (CNA) can be used for *in vivo* applications, where a micro- or nano-robot may be used to transport the sensing platform, thus avoiding the need for bulky lenses and cameras. This paper use our implementation of the our MLFMA [11, 12] as the vehicle to explore the electromagnetic scattering of the RBC solutions.

The rest of the paper was divided as follows. Section II explains the morphology of healthy and anomalous RBCs, including mesh details for the RBCs models inputed to the MLFMA code. Then, in Section III, the proposed methods based on conventional scattering measurements on multiple-RBC samples are introduced. Section IV addresses the 3D imaging problem using a CNA.

II. MORPHOLOGY AND MODELING OF RBCS

In order acurately model a realistic blood samples, the position and orientation of each RBC is determined randomly. Specifically, several uniform random distributions were used to define the position and the two independent rotations along
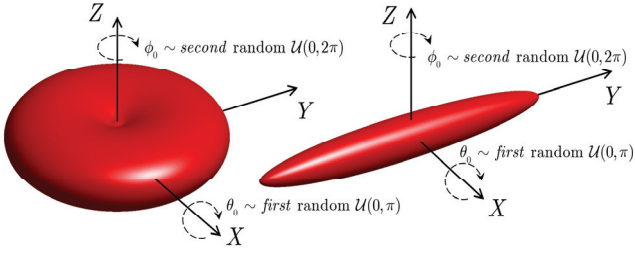
Fig. 1. Reference Cartesian axes used in this work, and illustration of two random rotations, modeled as uniform distributions, around X and Z axes.
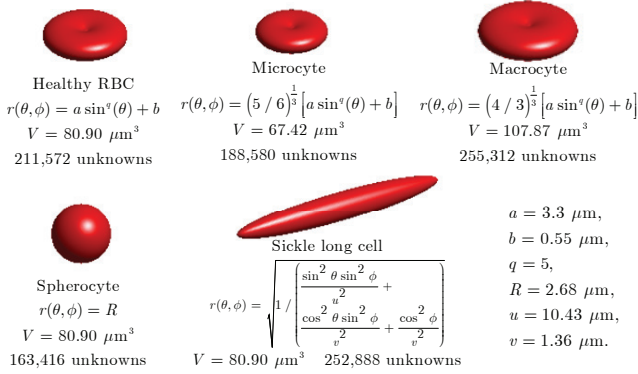

Fig. 2. Healthy and diseased RBC models, indicating equation for the membrane, volume, and number of simulated unknowns per cell.

the two axes shown in Fig. 1. Five different types of RBC are studied in this work (see Fig. 2): healthy RBCs, and four anomalous types of RBCs. The underlying disease and disorders for each one of the four anomalous types of RBC are described in [1,3]. The equations used to model the cell surface were extracted from [3], except for the sickle long cell, which was inferred from data in [1,3]. All the triangular meshes of RBCs were created in the free mesh generator software Gmsh [13], selecting $\ell_{discr} = \lambda_{0,min}/10$ as the maximum edge size for the triangles.

In our MLFMA implementation, we used local Lagrange interpolation with 6 points for interpolating between consecutive levels, a block size of $0.5\lambda_0$ for the finest level, and an ILU(0) preconditioner as described in subsection 9.6.3 of [6]. Our computational implementation of the MLFMA method consists of a regular C code involving double-precision floating-point calculations, and we have employed ordinary RWG functions [6] and a 7-point Gaussian quadrature rule for numerical integration over each triangular facet. The GMRES iterative solver, with restart 100 and residual tolerance 10^{-3}, was chosen for the iterative solutions via MLFMA. Finally, the simulations solved with the MLFMA were formulated using the electric and magnetic current combined-field integral equation (JMCFIE). This formulation was chosen as it provides well-conditioned equations for probems involving low-contrast [3] (i.e., the permittivities of RBCs and surrounding plasma are similar), and it allows a fast iterative convergence of the scattering pattern produced by the Compressive Nano-Antenna

TABLE I
SUMMARY OF RCS DISCRIMINATION RULES ACCORDING TO FIG. 3

Cell type	Discrimination criteria: $\phi = 0°$, $\theta \in [-45°, 45°]$
Healthy RBCs	$-5 < mean(RCS) < 0$ dBμm^2
Microcytes	$-10 < mean(RCS) < -5$ dBμm^2
Macrocytes	0 dBμm$^2 < mean(RCS)$
Spherocytes	$mean(RCS) < -10$ dBμm^2
Sick long RBCs	$-5 < mean(RCS) < 0$ dBμm^2

[11,12].

III. HEMATOLOGIC CHARACTERIZATION OF RBCs

This section describes two methodologies for the hematologic characterization of RBCs having different disorders using scattered field data. The first of them employs bistatic radar cross section (RCS) measurements at a single frequency, whilst the second sub-method performs scattering cross section (SCS) spectroscopy measurements spanning an optical frequency range. Before measurement, a blood sample with 50 RBCs is insulated into a $70 \times 70 \times 5$ μm container. This operation can be easily performed by a classical flow cytometer. It is worth noting that, however, a classical microscopy technique can lead to issues when discriminating among healthy RBCs, microcytes and macrocytes. All the presented results correspond to an average over 20 different samples, i.e., 1000 sampled cells. RBCs are illuminated by a plane wave $\mathbf{E}_{inc}(r) = e^{j\frac{2\pi}{\lambda_0}z}\hat{\mathbf{x}}$. Relative permittivities of the RBCs and the surrounding medium were respectively defined as $\epsilon_{RBC} = 1.40$ and $\epsilon_{plasma} = 1.33$ [3].

A. Discrimination using the radar cross section

For this subsection, numerical simulations are performed at 474 THz, which corresponds to the output frequency of a typical HeNe laser. Fig. 3 shows, for each cell type, a picture of the simulated geometries, the near field results and RCS values obtained according to (1), using the scattered field $\mathbf{E}_{scat}$:

$$RCS(\theta, \phi) = \lim_{r \to \infty} \left[4\pi r^2 \frac{|\mathbf{E}_{scat}(r, \theta, \phi)|^2}{|\mathbf{E}_{inc}|^2} \right]. \quad (1)$$

The RCS results in Fig. 3 are summarized in Table I in order to extract discrimination rules according to the numerical simulation outcomes. It is worth noting that the distinction between healthy and long RBCs is quite problematic using the simulated mean values in Fig. 3. For this purpose, one can employ the procedure in the following subsection.

B. Discrimination using the scattering cross section

For an incident plane wave, the scattering cross section (σ_s) can be calculated from the incident ($\mathbf{E}_{inc}$, $\mathbf{H}_{inc}$) and scattered ($\mathbf{E}_{scat}$, $\mathbf{H}_{scat}$) fields by numerically integrating over an arbitrary surface S_0 enclosing each blood sample as [14]

$$\sigma_s = \frac{\oint_{S_0} \frac{1}{2}\text{Re}(\mathbf{E}_{scat} \times \mathbf{H}_{scat}^*) \cdot d\mathbf{s}}{\frac{1}{2}|\text{Re}(\mathbf{E}_{inc} \times \mathbf{H}_{inc}^*)|}. \quad (2)$$

The values of σ_s were computed now in the wavelength range between 450 and 1000 nm, for the same blood samples defined
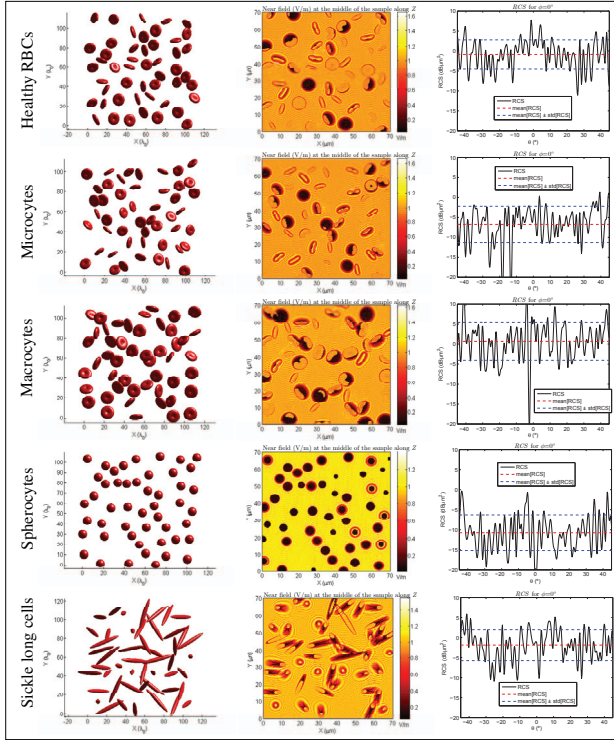
Fig. 3. Representation of simulated geometries for each RBC type, near field at the middle of the sample along Z, and bi-static RCS plots for the sweep range $\phi = 0°$, $\theta \in [-45°, 45°]$. Near field values inside the RBCs are scaled down by a factor of 6 for visual clarity purposes.
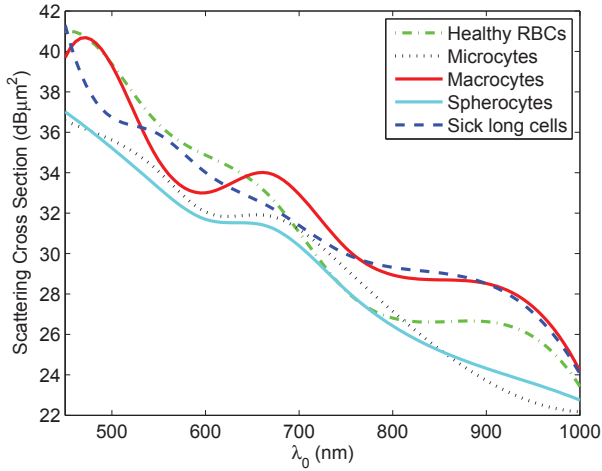

Fig. 4. Simulated light-spectroscopy measurements: averaged scattering cross sections (SCS) for 20 different RBC samples with 50 RBCs per sample.

in III.A. In this case, the visual comparison of the results in Fig. 4 allows unambiguously classifying different RBC types.

IV. 3D IMAGING OF RED BLOOD CELLS AFFECTED BY DIFFERENT DISORDERS USING A COMPRESSIVE NANO-ANTENNA

The 3D imaging using a Compressive Nano-Antenna (CNA) substantially outperforms the technique described above. A

CNA is assembled at the micro- and/or nano- scale by modifying the radiation pattern of an array of nano-antennas using a pseudo-randomly distorted a large transmitting or reflecting structure. As a result, the CNA pseudo-randomly illuminates a broad imaging space using multidimensional sub-beam-like codes [9–10]. Dynamically controlling these codes can ultimately enhance the sensing capacity (information transfer-efficiency between the imaging domain and measured data), and, therefore, the performance, of such a next generation sensing and imaging system. By exploiting such a multidimensional codification and leveraging on novel Compressive Sensing (CS) algorithms, the CRNA sensing platform is capable of 3D reconstruction of the RBCs' membrane shape. Moreover, the instrumental required for its implementation makes it suitable to be used in *in vitro* and *in vivo* nano-robot measurements.

CS theory was first introduced by Candès et al. in [15]. Since them, this theory has been refined by others. A good review in CS theory is presented in [16] and references therein. CS establishes that sparse signals can be recovered in *a priori* **undetermined** linear complex-valued systems $\mathbf{g} = \mathbf{H} \cdot \mathbf{r} + \mathbf{w}$ ($\mathbf{w}$ is measurement noise) if certain mathematical conditions are met by the sensing matrix $\mathbf{H}$ and the reconstructed image $\mathbf{r}$. Matrix $\mathbf{H}$ must satisfy the so-called restricted-isometry-property (RIP) condition, which is related with a low coherence of the matrix and can be achieved with the independence of the columns [15]. Another condition requires that the number of nonzero entries in $\mathbf{r}$ be much smaller than its total number of elements. If the two aforesaid conditions are satisfied, then the reconstruction of the unknown vector $\mathbf{r}$ is achievable with a small number of measurements by solving the following optimization problem:

$$\min \|\mathbf{r}\|_1 \quad \text{s.t.} \quad \|\mathbf{H} \cdot \mathbf{r} - \mathbf{g}\|_2 \leq \delta_H, \qquad (3)$$

where δ_h is an upper bound for the residual error, and $\|\|_1$ and $\|\|_2$ respectively denote the 1-norm and 2-norm. In our particular simulations, we used $\delta_h = 10^{-4}$.

A. System concept of operation and sensing matrix

Our designed system consists of 6 Yagi-Uda plasmonic nano-antennas with metallic compositions described over Fig. 5. The baseline design for each nano-antenna can be found in [17]. The antennas are embedded into a dielectric substrate made of two crystal pieces as shown in Fig. 5, which are pseudo-randomly distorted, thus assembling the CNA. The random surface of the CNA was modeled as described in Fig. 6. First, a mesh with $\ell_{discr} = \lambda_{0,min}$ ($\lambda_{0,min}$ is the minimum simulated wavelength) was generated. Then, a uniformly random deviation indicated in Fig. 6 was introduced in the original mesh triangle vertices; and, afterwards, the complete original triangles were re-meshed at $\ell_{discr} = 0.08\lambda_{0,min}$. The method in [18, 19] was employed to model the material junctions when simulating.

The system works on a multiple mono-static configuration, in which each element of the array transmits and receives on
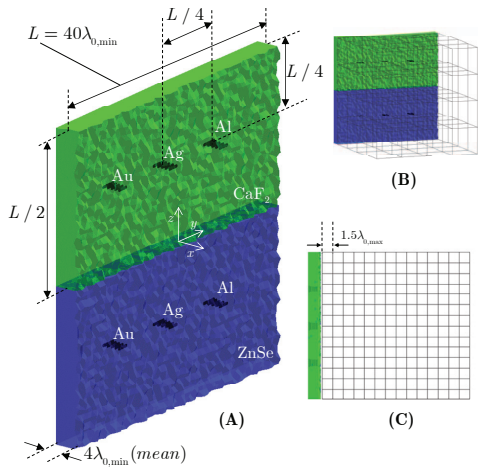
Fig. 5. Simulated system for CS imaging, not at scale. (A) Two crystals of calcium fluoride (CaF_2) and zinc selenide (ZnSe) with 6 embedded metallic Yagi-Uda nano-antennas made of gold, silver and aluminum –the antenna design can be consulted in [17]–. (B) Near-field 3D region of interest (ROI) –for clarity, the number of pixels does not correspond to the actual number used in the simulations–. (C) 2D view of the ROI –the number of depicted pixels is 14^3, as in the simulations–.
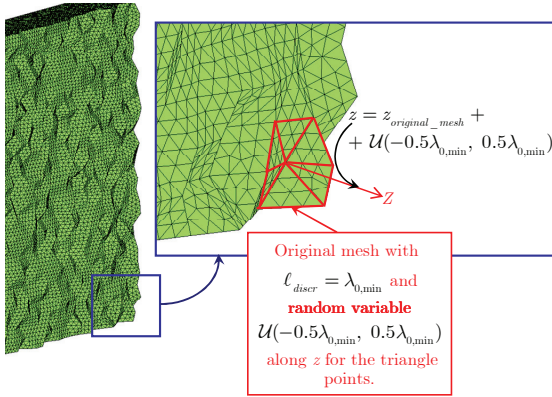

Fig. 6. Random mesh generation by re-meshing original triangles after introducing a uniformly distributed variation along Z.

different time slots. When each antenna is operating, a spatial random code is generated as seen in Fig. 7.

The sensing matrix, employed by the nano-imaging algorithm, is computed as follows: *1)* for each antenna $m_a \in \{1, ..., M_a\}$ and for each frequency $m_f \in \{1, ..., M_f\}$ a near-field simulation is realized (we used $M_a = 6$ antennas, and $M_f = 8$ equally spaced frequencies corresponding to the range between $\lambda_{0,max} = 1000$ nm and $\lambda_{0,min} = 500$ nm, both ends included); *2)* the simulated near field is used to illuminate an infinitesimal sphere located at the center of every pixel n_p in the region of interest (ROI) shown in Fig. 5; *3)* the backscattered field by each sphere, $\mathbf{E}(m_a, m_f, n_p)$, is computed at each antenna feeding element. Since we operate at the optical domain, the light intensity $|\mathbf{E}(m_a, m_f, n_p)|^2$ is stored as the coefficient h_{ij} of the sensing matrix $\mathbf{H}$, where $i = (m_a - 1)M_f + m_f$ and $j = n_p$. In our particular system, matrix $\mathbf{H}$ has dimensions 48×14^3.
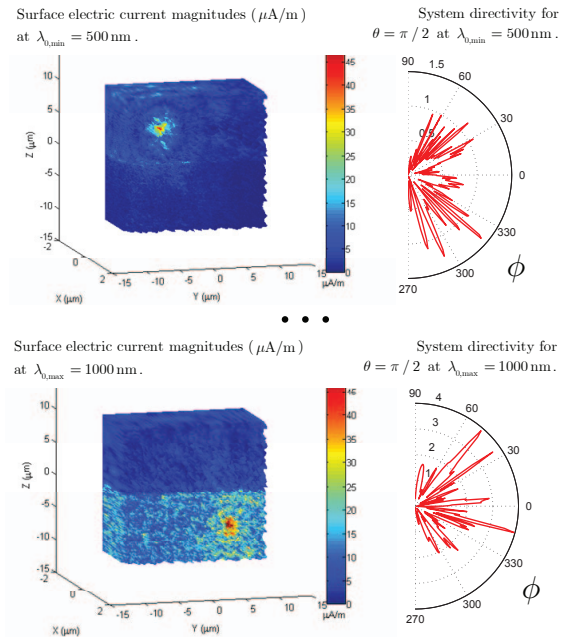

Fig. 7. Surface electric currents and random directivity patterns for two antennas: gold at $\lambda_{0,min}$ (top) and aluminum at $\lambda_{0,max}$ (bottom). Even though the CS simulation is performed in the near-field ROI, the directivity patterns allow for assessment of the random behavior.

B. Imaging algorithm using the compressive sensing approach

The proposed system was designed in accordance with the compressive sensing theory. Nevertheless, the RBC shapes typically lead to unknown image vectors $\mathbf{r}$ that are not sparse, thus stultifying the efforts to solve the CS optimization problem in (3). If $\mathbf{r}$ is not sparse, the problem can still be solved using the total variation (TV) norm: [20]:

$$\min \|\mathbf{r}\|_{\mathrm{TV}} \quad \text{s.t.} \quad \|\mathbf{H} \cdot \mathbf{r} - \mathbf{g}\|_2 \le \delta_H, \tag{4}$$

where the TV-norm $\|\|_{\mathrm{TV}}$ is defined using the 2-norm $\|\|_2$:

$$\|\mathbf{r}\|_{\mathrm{TV}} = \sum_{i,j,k} \|\nabla \mathbf{r}_{i,j,k}\|_2, \quad \nabla \mathbf{r}_{i,j,k} = \begin{bmatrix} \mathbf{r}_{i+1,j,k} - \mathbf{r}_{i,j,k} \\ \mathbf{r}_{i,j+1,k} - \mathbf{r}_{i,j,k} \\ \mathbf{r}_{i,j,k+1} - \mathbf{r}_{i,j,k} \end{bmatrix}. \tag{5}$$

$\nabla \mathbf{r}_{i,j,k}$ represents the discrete gradient and i, j, k are 3D discrete spatial indices for each pixel. Once obtained the sensing matrix $\mathbf{H}$ and the measurement vector $\mathbf{g}$ via CEM simulations in C, we used the MATLAB® toolbox NESTA v.1.1 [20] to solve (4). Even though NESTA only includes the TV-norm optimization for the 2D case, it can be generalized to 3D using the recent procedure in [21].

Fig. 8 shows a reconstruction example involving a healthy RBC with $SNR = 25$ dB. For SNR values above 25 dB, it was required to define a threshold of about 0.75 in the reconstructed pixels, i.e., we only consider $|\mathbf{r}_{i,j,k}| > 0.75$, for a clear reconstruction of RBC shapes. Fig. 9 includes original results without applying the threshold. Finally, Fig. 10 shows another reconstruction example, where the membrane of a sickle long cell is reconstructed.
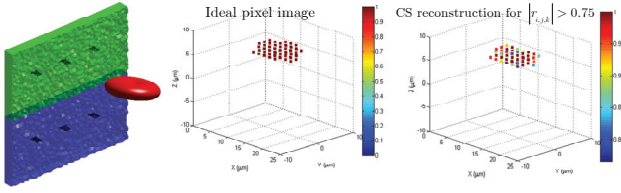
Fig. 8. CS reconstruction for a healthy normal RBC: (left) problem representation; (middle) ideal pixel image; (right) CS reconstruction with threshold $|\mathbf{r}_{i,j,k}| > 0.75$.
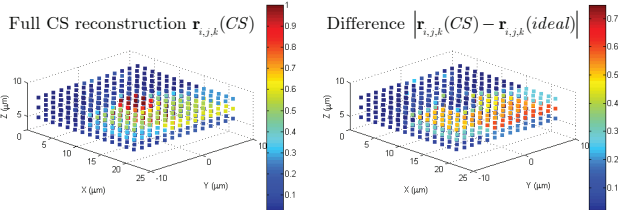

Fig. 9. CS reconstruction for a healthy normal RBC: (left) CS reconstruction without threshold; (right) difference between ideal and reconstructed pixels.

REFERENCES

[1] J. Q. Lu, P. Yang, and X.-H. Hu, "Simulations of light scattering from a biconcave red blood cell using the finite-difference time-domain method," *Journal of Biomedical Optics,* vol. 10, no. 2, 2005.

[2] L. Bi and P. Yang, "Modeling of light scattering by biconcave and deformed red blood cells with the invariant imbedding T-matrix method," *Journal of Biomedical Optics,* vol. 18, no. 5, 2013.

[3] Ö. Ergül, A. Arslan-Ergül, and L. Gürel, "Computational study of scattering from healthy and diseased red blood cells," *Journal of Biomedical Optics,* vol. 15, no. 4, 2010.

[4] K. Lee, K. Kim, J. Jung, J. Heo, S. Cho, S. Lee, G. Chang, Y. Jo, H. Park, and Y. Park, "Quantitative phase imaging techniques for the study of cell pathophysiology: from principles to applications," *Sensors* (ISSN 1424–8220), vol. 13, pp. 4170–4191, 2013.

[5] Ö. Ergül and L. Gürel, *The Multilevel Fast Multipole Algorithm (MLFMA) for Solving Large-Scale Computational Electromagnetics Problems,* IEEE Press, 2014.

[6] W. C. Gibson, *The Method of Moments in Electromagnetics, 2nd ed,* Chapman & Hall / CRC, 2014.

[7] Y. Rodriguez-Vaqueiro, Y. Alvarez-Lopez, B. Gonzalez-Valdes, J. A. Martinez-Lorenzo, F. Las-Heras, and C. M. Rappaport, "On the use of compressed sensing techniques for improving multistatic millimeter-wave portal-based personnel screening," *IEEE Trans. Antennas Propagat.,* vol. 62, no. 1, pp. 494–499, 2014.

[8] B. Gonzalez-Valdes, G. Allan, Y. Rodriguez-Vaqueiro, Y. Alvarez, S. Mantzavinos, M. Nickerson, B. Berkowitz, J. A. Martinez-Lorenzo, F. Las-Heras, and C. M. Rappaport, "Sparse array optimization using simulated annealing and compressed sensing for near-field millimeter wave imaging," *IEEE Trans. Antennas Propagat.,* vol. 62, no. 4, pp. 1716–1722, 2014.

[9] J. A. Martinez-Lorenzo, J. Heredia Juesas, and W. Blackwell, "A single-transceiver compressive reflector antenna for high-sensing-capacity imaging," *Antennas and Wireless Propagation Letters, IEEE,* vol. PP, no. 99, 2015.

[10] J. A. Martinez-Lorenzo, J. Heredia Juesas, and W. Blackwell, "Single-transceiver compressive antenna for high-capacity sensing and imaging applications," *Proceedings of the 2015 9th Conference on Antennas and Propagation (EuCAP),* April 13-17, 2015 in Lisbon, Portugal, 2015.

[11] H. Gomez-Sousa, O. Rubinos-Lopez, and J. A. Martinez-Lorenzo, "Comparison of iterative solver performances on multiple surface integral equation formulation for plasmonic scatterers," *Proceedings of the Antennas and Propagation Society International Symposium (APSURSI),* July 6-11, 2014 in Memphis, Tennessee, pp. 2116–2117, 2014.

[12] H. Gomez-Sousa, O. Rubinos-Lopez, and J. A. Martinez-Lorenzo, "Comparisons of iterative solvers for electromagnetic analysis of plasmonic nanostructures using multiple surface integral equation formulations," Unpublished in *Journal of Electromagnetic Waves and Applications.* arXiv pre-print available.

[13] C. Geuzaine and J.-F. Remacle, "Gmsh: a three-dimensional finite element mesh generator with built-in pre- and post-processing facilities," *Int. J. for Num. Methods in Eng.,* vol. 79, no. 11, pp. 1309–1331, 2009.

[14] D. M. Solis, J. M. Taboada, and F. Obelleiro, "Surface integral equation-method of moments with multiregion basis functions applied to plasmonics," *IEEE Trans. Antennas Propagat.,* vol. 63, no. 5, pp. 2141–2152, 2015.

[15] E. J. Candès, J. K. Romberg, and T. Tao, "Stable signal recovery from incomplete and inaccurate measurements," *Communications on pure and applied mathematics,* vol. 59, no. 8, pp. 1207-1223, 2006.

[16] A. Massa, P. Rocca, and G. Oliveri, "Compressive sensing in electromagnetics-a review," *Antennas and Propagation Magazine, IEEE,* vol. 57, no. 1, pp. 224-238, 2015.

[17] H. Gomez-Sousa, O. Rubinos-Lopez, and J. A. Martinez-Lorenzo, "Multilevel fast multipole algorithm with multiple octrees for the solution of large-scale plasmonic problems with junctions," *Proceedings of the 2015 9th Conference on Antennas and Propagation (EuCAP),* April 13-17, 2015 in Lisbon, Portugal, 2015.

[18] H. Gomez-Sousa, O. Rubinos-Lopez, and J. A. Martinez-Lorenzo, "Junction modeling for piecewise non-homogeneous geometries involving arbitrary materials," *Proceedings of the Antennas and Propagation Society International Symposium (APSURSI),* July 6-11, 2014 in Memphis, Tennessee, pp. 2196–2197, 2014.

[19] H. Gomez-Sousa, O. Rubiños-Lopez, and J. A. Martinez-Lorenzo, "A computational method for modeling arbitrary junctions employing different surface integral equation formulations for three-dimensional scattering and radiation problems," Unpublished in *Journal of Electromagnetic Waves and Applications.* arXiv pre-print available.

[20] S. Becker, J. Bobin, and E. J. Candès, "NESTA: a fast and accurate first-order method for sparse recovery," *SIAM Journal on Imaging Sciences,* vol. 4, no. 1, pp. 1-39, 2011.

[21] Y. Yao, J. Tang, P. Chen, S. Zhang, and J. Chen, "An improved iterative algorithm for 3-D ionospheric tomography reconstruction," *IEEE Trans. Geoscience and Remote Sensing,* vol. 52, no. 8, pp. 4696–4706, 2014.
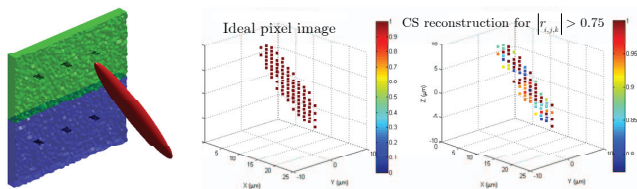
Fig. 10. CS reconstruction for a sickle long RBC: (left) problem representation; (middle) ideal pixel image; (right) CS reconstruction with threshold $|\mathbf{r}_{i,j,k}| > 0.75$.